

Near-Field Tapering with Slepian Window: Balancing the Range–Angle Sidelobe Trade-off

Ahmed Hussain, *Graduate Student Member, IEEE*, Ahmed Sultan, *Senior Member, IEEE*, Asmaa Abdallah *Member, IEEE*, Abdulkadir Celik, *Senior Member, IEEE*, and Ahmed M. Eltawil, *Senior Member, IEEE*

Abstract—Near-field beamforming enables target discrimination in both range (axial) and angle (lateral) dimensions. Elevated sidelobes along either dimension, however, increase susceptibility to interference and degrade detection performance. Conventional amplitude tapering techniques, designed for far-field scenarios, cannot simultaneously suppress axial and lateral sidelobes in near-field. In this letter, we propose a Slepian-based amplitude tapering approach that maximizes mainlobe energy concentration, achieving significant sidelobe reduction in both dimensions. Numerical results show that the proposed taper improves peak sidelobe suppression by approximately 24 dB in the lateral domain and 10 dB in the axial domain compared to a conventional uniform window.

Index Terms—Near-field, axial and lateral sidelobes, amplitude weighting, Slepian.

I. INTRODUCTION

SENSING, formally recognized as a key service in 3GPP release 20, is envisioned as a core capability of sixth generation (6G) wireless networks. This paradigm shift is driven by the adoption of millimeter wave (mmWave) bands, coupled with ultra-massive (UM)-multiple-input multiple-output (MIMO) architectures, that jointly enable fine spatial resolution through wide bandwidths and large antenna apertures, respectively [1]. At such scales, electromagnetic propagation occurs in the radiative near-field (NF) regime, where spherical wavefronts enable the formation of NF beams. These beams exhibit finite beamwidth and beamdepth, thereby facilitating target resolution in both angular (lateral) and range (axial) domains. However, unlike the far-field (FF), where interference arises solely from lateral sidelobes (LSLs), NF beams exhibit both axial sidelobes (ASLs) and LSLs, rendering them susceptible to interference in both axial and lateral dimensions.

Sidelobe suppression is critical for reliable sensing and secure communication, as the mainlobe width determines spatial resolution while sidelobe levels (SLLs) govern susceptibility to interference. Reducing sidelobes enhances sensing performance by mitigating undesired signal leakage from interference sources and improves multiuser communication performance by increasing the achievable sum rate. The overall lateral beam pattern depends on the product of the element pattern and array factor; hence, reducing element sidelobes directly lowers LSLs. Conversely, the element pattern does not influence the axial beam pattern. In the FF, amplitude weights are applied in the spatial domain to reduce LSLs in the angular domain [2]. In contrast, within the NF context, it is essential

The authors are with Computer, Electrical, and Mathematical Sciences and Engineering (CEMSE) Division, King Abdullah University of Science and Technology (KAUST), Thuwal, 23955-6900, KSA.

to investigate how a single set of amplitude weights (in the spatial domain) can simultaneously suppress both ASL and LSL. Recent findings reveal a fundamental trade-off between ASL and LSL suppression: optimizing tapering weights for one domain often degrades performance in the other [3], [4]. This inherent coupling raises a critical research question: *Can we design an amplitude distribution that jointly minimizes ASL and LSL?*

Interestingly, the trade-off between ASL and LSL suppression mirrors the classical time–frequency uncertainty, in which a signal cannot be simultaneously time-limited and band-limited. Slepian sequences address this by maximizing the energy concentration of a finite-length sequence within a prescribed bandwidth [5]. These sequences are mutually orthogonal, and the principal Slepian sequence yields the most effective window function for sidelobe suppression. Drawing on this analogy, the NF problem exhibits a similar duality, as range and angle domains are inherently coupled with unavoidable resolution trade-offs. Motivated by this parallel, in this letter we first characterize the NF beam patterns across the range–angle domain and quantify the underlying trade-offs. We then propose Slepian-based amplitude tapers for NF beamforming that jointly suppress ASL and LSL, yielding superior performance compared to existing windowing methods.

II. SYSTEM MODEL

In this section, we present the NF beam pattern and specify the metrics to quantify the SLLs.

A. Channel Model

We consider a uniform linear array (ULA) equipped with N isotropic antenna elements spaced $d = \lambda/2$. Based on the planar wavefront assumption, the normalized FF array response vector $\mathbf{a}(\theta) \in \mathbb{C}^{N \times 1}$ is formulated as

$$\mathbf{a}(\theta) = \frac{1}{\sqrt{N}} \left[1, e^{-j\nu d \sin(\theta)}, \dots, e^{-j\nu d(N-1) \sin(\theta)} \right]^T, \quad (1)$$

where $\nu = \frac{2\pi}{\lambda}$ is the wavenumber, and λ is the wavelength. On the other hand, the NF array response vector $\mathbf{b}(\theta, r) \in \mathbb{C}^{N \times 1}$ based on the spherical wave model is given by

$$\mathbf{b}(\theta, r) = \frac{1}{\sqrt{N}} \left[e^{-j\nu(r^{(0)}-r)}, \dots, e^{-j\nu(r^{(N-1)}-r)} \right]^T, \quad (2)$$

where r is the distance between the focal point and the center of the ULA, while $r^{(n)}$ is the distance between the focal point and the n^{th} antenna element. The corresponding phase shift $\nu(r^{(n)}-r)$, obtained via the law of cosines, is expressed as $\nu(r^{(n)}-r) = \frac{2\pi}{\lambda} \left(\sqrt{r^2 + n^2 d^2 - 2rnd \sin(\theta)} - r \right)$. Accordingly, n^{th} component of the NF array response vector can be written as

$$b_n(\theta, r) = \frac{1}{\sqrt{N}} e^{-j\nu \sqrt{r^2 + n^2 d^2 - 2rnd \sin(\theta)} - r}. \quad (3)$$

The above equation can be simplified by using *near field expansion* based on the second-order Taylor expansion as $\sqrt{1+t} \approx 1 + \frac{t}{2} - \frac{1}{8}t^2$ where $\sqrt{r^2 + n^2 d^2 - 2r n d \sin(\theta)} - r \approx n d \sin(\theta) - \frac{1}{2r} n^2 d^2 \cos^2(\theta)$. Hence, $b_n(\theta, r)$ in (3) is approximated as

$$b_n(\theta, r) \approx \frac{1}{\sqrt{N}} e^{-j\nu\{nd\sin(\theta) - \frac{1}{2r}n^2d^2\cos^2(\theta)\}}. \quad (4)$$

B. Problem Formulation

The NF beam pattern is obtained by applying the complex weights \mathbf{g} to the antenna elements as

$$\mathcal{G}(\theta, r) = |\mathbf{g}^H(\theta_0, r_0) \mathbf{b}(\theta, r)|^2, \quad (5)$$

where (θ_0, r_0) denotes the desired beamfocusing location in angle and range, respectively. The weighting vector \mathbf{g} can be decomposed into element-wise amplitude and phase components as

$$\mathbf{g} = \mathbf{w} \odot e^{j\phi}, \quad (6)$$

where \mathbf{w} is the real-valued amplitude vector, $e^{j\phi}$ is the complex phase vector, and \odot denotes the Hadamard (element-wise) product. In general, the phase component focuses the beam toward the desired location (θ_0, r_0) , while the amplitude component is designed to control the SLL. For a given focus point, the phase component $e^{j\phi}$ is obtained using (4). Substituting the decomposition of \mathbf{g} from (6) into the beam pattern expression in (5) yields

$$\mathcal{G}(\theta, r) = |(\mathbf{w} \odot \mathbf{b}(\theta_0, r_0))^H \mathbf{b}(\theta, r)|^2. \quad (7)$$

Given the peak of the mainlobe is $\mathcal{G}(\theta_0, r_0)$, the peak sidelobe level (PSLL) and integrated sidelobe level (ISLL) are defined as follows:

a) **PSLL:** The PSLL quantifies the ratio of the highest sidelobe magnitude to the mainlobe peak, indicating worst-case sidelobe susceptibility against narrowband interference.

$$\text{PSLL} = 10 \log_{10} \left(\frac{\max_{(x) \in \mathcal{S}} \mathcal{G}(\theta, r)}{\mathcal{G}(\theta_0, r_0)} \right), \quad (8)$$

where x denotes either angle (θ) or range (r) depending on the domain of interest. \mathcal{S} corresponds to the set of points in the sidelobe region.

b) **ISLL:** The ISLL quantifies the ratio of the total sidelobe power to the mainlobe power, characterizing the beampattern's susceptibility against wideband interference.

$$\text{ISLL} = 10 \log_{10} \left(\frac{\int_{\mathcal{S}} |\mathcal{G}(\theta, r)|^2 dx}{\int_{\mathcal{M}} |\mathcal{G}(\theta, r)|^2 dx} \right), \quad (9)$$

where \mathcal{M} corresponds to the mainlobe. Fig. 1 illustrates the mainlobe and sidelobe regions, as well as the PSLL, for a NF beam pattern in the range domain. Conventional window designs entail a trade-off between ASL and LSL suppression, as detailed in Section III-D. To address this limitation, we propose a window that jointly attenuates both ASL and LSL in terms of PSLL and ISLL.

III. BEAM PATTERN ANALYSIS

In this section, we derive the beamwidth, beamdepth, and PSLL of the NF beam in both the angular and range domains, assum-

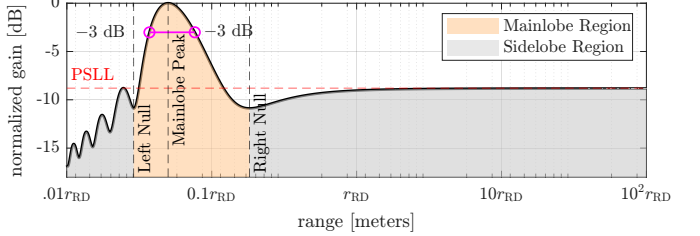


Fig. 1: NF beam pattern with mainlobe and .

ing uniform amplitude excitation $\mathbf{w} = \mathbf{1}$. We then highlight the inherent range-angle trade-off in sidelobe suppression.

A. Angle-Domain

To evaluate the beam pattern in the angular domain, we consider a distance ring defined by $\frac{\cos^2(\theta)}{r} = \frac{\cos^2(\theta_0)}{r_0}$ [6]. This curve corresponds to a set of range-angle pairs over which the beamwidth remains approximately invariant. Accordingly, the beam pattern in the angle domain can be expressed as

$$\begin{aligned} \mathcal{G}(\theta) &= |\mathbf{b}^H(\theta_0, r_0) \mathbf{b}(\theta, r)|^2, \\ &\approx \left| \frac{1}{N} \sum_{n=0}^{N-1} e^{j\nu n d (\sin \theta - \sin \theta_0)} e^{-j\nu \frac{n^2 d^2}{2} \left(\frac{\cos^2 \theta}{r} - \frac{\cos^2 \theta_0}{r_0} \right)} \right|^2, \\ &\stackrel{(a)}{=} \left| \frac{1}{N} \sum_{n=0}^{N-1} e^{j\nu n d (\sin \theta - \sin \theta_0)} \right|^2, \\ &= \left| \frac{1}{N} \frac{\sin\left(\frac{N\nu d}{2}(\sin \theta - \sin \theta_0)\right)}{\sin\left(\frac{\nu d}{2}(\sin \theta - \sin \theta_0)\right)} \right|^2, \end{aligned} \quad (10)$$

where (a) follows from the relation $\frac{\cos^2(\theta)}{r} = \frac{\cos^2(\theta_0)}{r_0}$. From (10), half power beamwidth (HPBW) $\Delta\theta_{3\text{dB}}$ is derived as

$$\Delta\theta_{3\text{dB}} \approx \frac{0.886\lambda}{Nd \cos \theta_0}, \quad (11)$$

which is identical to the HPBW expression in the FF [7]. The PSLL of a uniformly weighted array is determined by the secondary maxima of the gain function $\mathcal{G} = \left| \frac{\sin\left(\frac{N}{2}x\right)}{N \sin(x/2)} \right|^2$ in (10), where $x = \nu(\sin \theta - \sin \theta_0)d$. The mainlobe attains its peak value of unity at $x = 0$, while the first sidelobe occurs at $x \approx 3\pi/N$, yielding $\text{PSLL} \approx 10 \log_{10}(1/(3\pi/2)^2) \approx -13.46$ dB, where a *small angle* approximation is applied in the denominator to obtain $\sin(\frac{3\pi}{2N}) \approx \frac{3\pi}{2N}$.

B. Range-Domain

The beam pattern in the range domain is obtained as the inner product of NF array response vectors pointing to the same angle θ but different distances r and r_0 [8]

$$\mathcal{G}(\theta, r) = |\mathbf{b}^H(\theta, r_0) \mathbf{b}(\theta, r)|^2, \quad (12)$$

$$\stackrel{(a)}{=} \left| \frac{1}{N} \sum_{n=-N/2}^{N/2} e^{-j\nu n^2 d^2 \cos^2(\theta) r_{\text{eff}}} \right|^2, \quad (13)$$

$$\stackrel{(b)}{\approx} \frac{C^2(\gamma) + S^2(\gamma)}{\gamma^2}, \quad (14)$$

where $r_{\text{eff}} = \left| \frac{r-r_0}{2rr_0} \right|$ in (a). By introducing the transformation $x = \sqrt{\frac{n^2 d^2 \cos^2(\theta)}{\lambda}} \left| \frac{r-r_0}{rr_0} \right|$, $\mathcal{G}(\theta, r)$ is expressed in terms of

TABLE I: Angular vs. range domain beam pattern.

Property	Angular Domain	Range Domain
Beam Pattern	Sinc	Fresnel
Symmetry	Symmetric about θ_0	Asymmetric about r_0
PSLL	-13.46 dB	-8.7 dB
Grating Lobes	Present (sinc periodicity)	Absent (non-periodic)

Fresnel functions in (b), where $\gamma = \sqrt{\frac{N^2 d^2 \cos^2(\theta)}{\lambda} r_{\text{eff}}}$. Furthermore, $C(\gamma) = \int_0^\gamma \cos\left(\frac{\pi}{2}x^2\right) dx$, $S(\gamma) = \int_0^\gamma \sin\left(\frac{\pi}{2}x^2\right) dx$ are the Fresnel cosine and sine integrals.

Half power beamdepth (HPBD) r_{BD} is defined as the distance interval $r \in [r_0^{\text{min}}, r_0^{\text{max}}]$ where normalized array gain is at most 3 dB lower than its maximum value. For a ULA, [9]

$$r_0^{\text{min}} = \frac{r_0 r_{\text{RD}} \cos^2(\theta)}{r_{\text{RD}} \cos^2(\theta) + 4r_0 \alpha_{3\text{dB}}}, \quad (15)$$

$$r_0^{\text{max}} = \frac{r_0 r_{\text{RD}} \cos^2(\theta)}{r_{\text{RD}} \cos^2(\theta) - 4r_0 \alpha_{3\text{dB}}}, \quad (16)$$

where $r_{\text{RD}} = \frac{2D^2}{\lambda}$ is the Rayleigh distance and D represents the aperture length of the ULA. Based on (15) and (16), $r_{\text{BD}} = r_0^{\text{max}} - r_0^{\text{min}}$ is given by

$$r_{\text{BD}} = \begin{cases} \frac{8\alpha_{3\text{dB}} r_0^2 r_{\text{RD}} \cos^2(\theta)}{(r_{\text{RD}} \cos^2(\theta))^2 - (4\alpha_{3\text{dB}} r_0)^2}, & r_0 < \frac{r_{\text{RD}}}{4\alpha_{3\text{dB}}} \cos^2(\theta), \\ \infty, & r_0 \geq \frac{r_{\text{RD}}}{4\alpha_{3\text{dB}}} \cos^2(\theta), \end{cases} \quad (17)$$

where $\alpha_{3\text{dB}} \triangleq \{\gamma \mid \mathcal{G}(\theta, r) = 0.5\}$ denotes the value of γ , where $\mathcal{G}(\theta, r)$ reduces to half. Furthermore, $\frac{r_{\text{RD}}}{4\alpha_{3\text{dB}}} \cos^2(\theta)$ defines the maximum range limit beyond which r_{BD} goes to infinity.

To find the PSLL in the range domain, we solve $\frac{d}{d\gamma} \left(\frac{C^2(\gamma) + S^2(\gamma)}{\gamma^2} \right)$. Solving numerically, the peak of the first sidelobe occurs at $\gamma_{\text{PSLL}} \approx 2.28$, with $\mathcal{G}(\gamma_{\text{PSLL}}) \approx 0.1323$, giving a PSLL of $10 \log_{10}(0.1323) = -8.7$ dB, which is also highlighted as red dotted line in Fig. 1.

C. Range vs. Angle Beam Pattern

The key differences between the axial and lateral beam patterns are summarized in Table I. Notably, the angular pattern is symmetric about the steering angle θ_0 , whereas the range pattern is asymmetric, as observed from (15) and (16), with $|r_0^{\text{max}} - r_0| > |r_0 - r_0^{\text{min}}|$. As derived in Sections III-A and III-B, the PSLL in the range domain is approximately 5 dB higher than that in the angular domain. Furthermore, the periodicity of the sinc function introduces grating lobes in the angular domain when $d > \frac{\lambda}{2}$. In contrast, the Fresnel function is aperiodic, and therefore the range pattern does not exhibit any grating lobes.

D. Range-Angle Trade-off

The FF beam provides lateral resolution, i.e., the ability to distinguish targets at the same range but different angles. The NF beam additionally enables axial resolution, i.e., the ability to distinguish targets at the same angle but different ranges. At short ranges, the beamdepth becomes extremely narrow, whereas the Fourier transform-based angular resolution degrades significantly. Conversely, at larger distances or wider angles, the lateral resolution improves while the axial resolution deteriorates due to the increased beamdepth [9, Fig. 1]. This trade-off is analogous to the time-frequency uncertainty, which prevents a function from being simultaneously localized in both domains. Consequently, conventional window functions cannot achieve simultaneous sidelobe suppression across both dimensions.

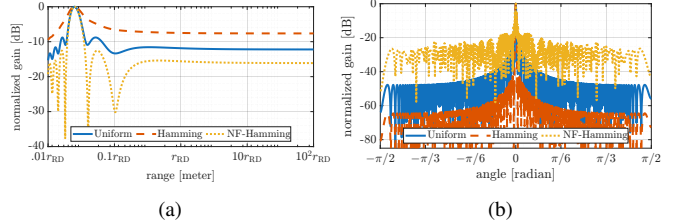


Fig. 2: (a) The NF-Hamming window effectively suppresses the ASLs, while (b) the conventional Hamming window effectively suppresses the LSLs.

Standard FF techniques apply amplitude tapering as $\mathbf{a}(\theta) \odot \mathbf{w}(n)$, where $\mathbf{w}(n)$ suppresses only the LSL. To address this limitation, a transformation is proposed in [3], which maps a conventional window $\mathbf{w}(n)$ to a modified window $\bar{\mathbf{w}}(n)$, thereby enabling existing designs to be directly adapted for ASL suppression

$$\bar{\mathbf{w}}(n) = |n| \mathbf{w}(n^2). \quad (18)$$

To illustrate further, Fig. 2 compares ASL and LSL for three window functions: a uniform (untapered) case, a conventional Hamming window $\mathbf{w}(n)$, and its NF-Hamming $\bar{\mathbf{w}}(n)$ obtained from (18). As observed, the conventional Hamming window effectively suppresses LSL but increases ASL, whereas the NF-Hamming window reverses this trade-off by enhancing ASL suppression at the cost of higher LSL, even exceeding that of the uniform window.

IV. PROPOSED SLEPIAN-BASED WINDOW FUNCTION

In this section, we first review the classical Slepian window and then present the proposed window design.

A. Primer on Slepian Window

Slepian window achieves optimal trade-off between time and frequency resolutions for a given time-bandwidth product (NW) by maximizing the fraction of their total spectral energy within a specified band $[-W, W]$, where $0 < W < f_s/2$ and f_s is the sampling frequency. Let $s(n)$ denote the Slepian sequence in the time domain, and $S(f)$ its Fourier transform, given by $S(f) = \sum_{n=0}^{N-1} s(n) e^{-j2\pi f n T_s}$, where $T_s = 1/f_s$. The objective is to determine $s(n)$ that maximizes the energy concentration ratio given by [8]

$$\Lambda = \frac{\int_{-W}^W |S(f)|^2 df}{\int_{-f_s/2}^{f_s/2} |S(f)|^2 df}, \quad (19)$$

where $0 < \Lambda < 1$ is the concentration parameter. The above equation can be solved using Parseval's theorem to yield [5]

$$\Lambda = \frac{\sum_{n=0}^{N-1} \sum_{m=0}^{N-1} s(n)s(m) A_{n,m}}{\sum_{n=0}^{N-1} |s(n)|^2} = \frac{\mathbf{s}^\top \mathbf{A} \mathbf{s}}{\mathbf{s}^\top \mathbf{s}}, \quad (20)$$

where $A_{n,m} = \frac{2W}{f_s} \text{sinc}\left(\frac{2W}{f_s}(n-m)\right)$. The Rayleigh quotient in (20) attains its maximum when \mathbf{s} is the eigenvector associated with the largest eigenvalue of \mathbf{A} . This dominant eigenvector achieves maximal spectral concentration within the specified band $[-W, W]$ and serves as the Slepian window.

B. Proposed Slepian-based Window

We propose a Slepian-inspired optimization framework based on energy concentration within the desired mainlobe region

in the NF. This approach generalizes the classical Slepian concentration problem in (19) to a two-dimensional range-angle domain, yielding a solution expressed as a generalized Rayleigh quotient.

Let us consider a NF beam focused at (θ_0, r_0) , characterized by a finite beamwidth and beamdepth. We define the limits for the mainlobe power and the total power of the beam as follows: the *mainlobe power* is assumed to be primarily concentrated within the angular region $-\Delta\theta_{3\text{dB}}/2 \leq \theta \leq \Delta\theta_{3\text{dB}}/2$ and the range interval $r_0^{\min} \leq r \leq r_0^{\max}$, where r_0^{\min} and r_0^{\max} denote the beamdepth limits defined in (15) and (16), respectively, and $\Delta\theta_{3\text{dB}}$ is the 3dB beamwidth defined in (11). Furthermore, the *total beam power* in the range domain is confined within $r \in [r^{\min}, r^{\max}]$, where $r^{\min} = 0.62\sqrt{D^3/\lambda}$ denotes the inner boundary of the radiative NF region, and $r^{\max} = r_{\text{RD}}$ represents its outer boundary. In the angular domain, the beam is assumed to span $\theta \in [-\pi/2, \pi/2]$.

We recast (4) by defining $\Omega = \frac{d}{\lambda} \sin(\theta)$, which leads to $\cos^2(\theta) = 1 - \frac{\lambda^2 \Omega^2}{d^2}$. Accordingly, the n^{th} component of the NF array response vector can be expressed as

$$b_n(\Omega, r) = \frac{1}{\sqrt{N}} e^{-j2\pi\left(\Omega n - \frac{n^2 d^2}{2r\lambda} + \frac{\Omega^2 n^2 \lambda}{2r}\right)}, \quad (21)$$

Let w_n denote the n^{th} element of the desired window function. The Slepian-based concentration formulation, which maximizes the ratio of mainlobe power to total beam power, is given by ¹

$$\mathcal{J} = \frac{\int_{\Omega_{\min}}^{\Omega_{\max}} \int_{r_0^{\min}}^{r_0^{\max}} \left| \sum_{n=0}^{N-1} w_n^* b_n(\Omega, r) \right|^2 dr d\Omega}{\int_{-1/2}^{1/2} \int_{r^{\min}}^{r^{\max}} \left| \sum_{n=0}^{N-1} w_n^* b_n(\Omega, r) \right|^2 dr d\Omega}. \quad (22)$$

where $\Omega_{\min} = 0.5 \sin(-\Delta\theta_{3\text{dB}}/2)$, $\Omega_{\max} = 0.5 \sin(\Delta\theta_{3\text{dB}}/2)$ assuming $d = \frac{\lambda}{2}$. The numerator corresponds to power concentration within the desired mainlobe region, while the denominator integrates total power over the total spatial region. The goal is to maximize \mathcal{J} , analogous to maximizing spectral energy in a band in the classical Slepian problem. This leads to the following generalized Rayleigh quotient problem:

$$\mathcal{J} = \frac{\mathbf{w}^H \mathbf{A} \mathbf{w}}{\mathbf{w}^H \mathbf{B} \mathbf{w}}, \quad (23)$$

where \mathbf{A} and \mathbf{B} are $N \times N$ Hermitian matrices. The elements of \mathbf{A} are defined as

$$A_{n,m} = \int_{\Omega_{\min}}^{\Omega_{\max}} \int_{r_0^{\min}}^{r_0^{\max}} b_n(\Omega, r) b_m^*(\Omega, r) dr d\Omega, \quad (24)$$

and the elements of \mathbf{B} are given by

$$B_{n,m} = \int_{-1/2}^{1/2} \int_{r^{\min}}^{r^{\max}} b_n(\Omega, r) b_m^*(\Omega, r) dr d\Omega. \quad (25)$$

The above integrals are intractable to solve; therefore, approximate expressions for computing \mathbf{A} and \mathbf{B} are provided in Appendix A. The optimal weight vector \mathbf{w} that maximizes the concentration ratio \mathcal{J} in (23) is given by the *dominant generalized eigenvector* of the matrix pair (\mathbf{A}, \mathbf{B}) [10]. Specifically, it is the eigenvector associated with the largest generalized

¹ \star denotes conjugate operation.

eigenvalue λ , satisfying the generalized eigenvalue problem

$$\mathbf{A}\mathbf{w} = \lambda \mathbf{B}\mathbf{w}. \quad (26)$$

When both \mathbf{A} and \mathbf{B} are Hermitian and \mathbf{B} is positive definite, all generalized eigenvalues λ are real. Moreover, the eigenvectors $\{\mathbf{v}_i\}$ are mutually orthogonal under the inner product induced by \mathbf{B}

$$\mathbf{v}_i^H \mathbf{B} \mathbf{v}_j = 0, \quad i \neq j. \quad (27)$$

The magnitude of the n^{th} eigenvalue λ_n quantifies the energy concentration of the corresponding eigenvector \mathbf{v}_n . Therefore, the optimal tapering window is selected as the eigenvector corresponding to the largest eigenvalue

$$\mathbf{w} = |\mathbf{v}_{\max}|, \quad (28)$$

where $|\mathbf{v}_{\max}|$ denotes the magnitude of the dominant eigenvector. Note that the eigenvectors of the conventional Slepian sequence are real and mutually orthogonal. In contrast, in our case, the eigenvectors may be complex and are orthogonal with respect to the inner product defined by \mathbf{B} .

V. SIMULATION RESULTS

We consider a 128-element ULA operating at 15 GHz, with the NF beam focused at a range of $r_0 = \frac{r_{\text{RD}}}{100}$ and an angle of $\theta_0 = 0$. The NF array response vector is tapered using six window functions: the uniform window (no tapering), the conventional Hamming window, the NF-Hamming window derived from (18), and three variants of the proposed Slepian window. In the Slepian window design, the mainlobe limits act as tunable parameters that are adjusted to achieve the desired balance between ASL and LSL. In the Slepian-1 configuration, the angular ($\Omega_{\min}, \Omega_{\max}$) and range limits (r_0^{\min}, r_0^{\max}) of the mainlobe in (24) correspond to the 3 dB beamwidth and beamdepth obtained from (11), (15), and (16) respectively. In Slepian-2, the 3 dB beamwidth and beamdepth are enlarged by factors of 5 and 50, respectively, whereas in Slepian-3, these factors are further increased to 10 and 100.

As illustrated in Fig. 3, the Slepian-1 design exhibits behavior similar to the uniform window, as it is explicitly constructed to emulate its characteristics. The Slepian-2 configuration achieves ASL and LSL suppression levels comparable to those of the NF-Hamming and Hamming windows, respectively. The Slepian-3 window, however, surpasses both the Hamming and NF-Hamming benchmarks in overall performance.

To quantitatively substantiate these observations, Table II summarizes the PSLL and ISLL across both range and angular domains. The conventional Hamming window attains -33.17 dB LSL suppression but substantially degrades the axial response. Moreover, due to the absence of distinct nulls, identifying the PSLL becomes challenging. It is also noteworthy that other classical windows exhibit similar degradation in ASL suppression; hence, the Hamming window is selected here as a representative case. The NF-Hamming window provides -12.59 dB ASL suppression, while the LSLs rise to -3.73 dB. Its ISLL value of 2.97 dB further indicates that a considerable portion of the beam energy leaks into the sidelobes rather than remaining confined within the mainlobe.

Both the Slepian-2 and Slepian-3 designs achieve concurrent suppression of ASLs and LSLs. Specifically, the Slepian-2 window performs comparably to the Hamming window in

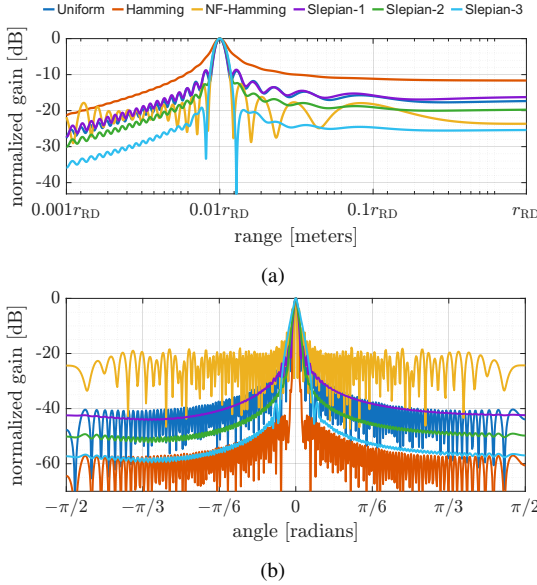


Fig. 3: Comparison of different windows in suppressing (a) ASLs in the range domain and (b) LSLs in the angular domain.

the angular domain and to the NF-Hamming window in the range domain. In terms of PSLL, it offers 5 dB lower LSL suppression than the Hamming window and 0.27 dB lower ASL suppression compared to the NF-Hamming window. The Slepian-3 configuration further enhances the performance of Slepian-2, providing 4.47 dB higher LSL suppression than the Hamming window and 6.58 dB greater ASL suppression relative to the NF-Hamming. The superior performance of Slepian-3 over Slepian-2, however, comes at the expense of increased beamwidth and beamdepth. This intrinsic trade-off between SLL suppression and mainlobe broadening is clearly reflected in Table II. Overall, the proposed Slepian-based tapers achieve a favorable balance by concentrating energy within the mainlobe while effectively suppressing sidelobes in both range and angular dimensions. Moreover, SLL attenuation in a specific domain can be flexibly tuned by adjusting the corresponding mainlobe boundaries, as demonstrated by the Slepian-2 and Slepian-3 designs.

VI. CONCLUSION

In this paper, we have proposed a Slepian-based amplitude tapering window to suppress ASLs and LSLs of the NF beam pattern. The proposed design maximizes energy concentration within the mainlobe to reduce the SLLs. Simulation results demonstrate that the proposed window effectively suppresses both ASLs and LSLs by adjusting the mainlobe limits. Future work includes exploring density-based array thinning strategies utilizing the proposed Slepian taper.

REFERENCES

- [1] A. Hussain, A. Abdallah, A. Celik, and A. M. Eltawil, “Near-field ISAC: Synergy of dual-purpose codebooks and space-time adaptive processing,” *IEEE Wireless Commun.*, vol. 32, no. 4, pp. 64–70, 2025.
- [2] S. Ogurtsov, D. Caratelli, and Z. Song, “A review of synthesis techniques for phased antenna arrays in wireless communications and remote sensing,” *Int. J. Antennas Propag.*, vol. 2021, no. 1, p. 5514972, 2021.
- [3] A. Hussain, A. Abdallah, A. Celik, E. Björnson, and A. M. Eltawil, “Analyzing URA geometry for enhanced near-field beamfocusing and spatial degrees of freedom,” *Submitted to IEEE Trans. Commun.*, 2024. [Online]. Available: <https://repository.kaust.edu.sa/handle/10754/706379>

TABLE II: Performance comparison of the window functions.

Window	PSLL [dB]		ISLL [dB]		Mainlobe	
	Range	Angle	Range	Angle	BD [m]	BW [deg]
Uniform	-8.98	-13.46	0.05	-8.24	0.24	0.85
Hamming	NA	-33.17	NA	-30.50	0.42	1.20
NF-Hamming	-12.59	-3.73	-4.26	2.97	0.27	0.85
Slepian-1	-8.48	-17.34	0.35	-12.24	0.25	1.32
Slepian-2	-12.32	-28.08	-3.60	-22.38	0.28	1.38
Slepian-3	-19.17	-37.64	-9.68	-33.09	0.29	1.84

- [4] W. Graham, “Analysis and synthesis of axial field patterns of focused apertures,” *IEEE Trans. Antennas Propag.*, vol. 31, no. 4, pp. 665–668, 1983.
- [5] D. Slepian, “Prolate spheroidal wave functions, fourier analysis, and uncertainty—v: The discrete case,” *Bell System Technical Journal*, vol. 57, no. 5, pp. 1371–1430, 1978.
- [6] H. Zhang, C. You, and C. Zhou, “Near-field beam-focusing pattern under discrete phase shifters,” *IEEE Trans. Wireless Commun.*, pp. 1–1, 2025.
- [7] H. L. Van Trees, *Optimum array processing: Part IV of detection, estimation, and modulation theory*. John Wiley & Sons, 2004.
- [8] A. Hussain, A. Abdallah, and A. M. Eltawil, “Redefining polar boundaries for near-field channel estimation for ultra-massive MIMO antenna array,” *IEEE Trans. Wireless Commun.*, pp. 1–1, 2025.
- [9] A. Abdallah, A. Hussain, A. Celik, and A. M. Eltawil, “Exploring frontiers of polar-domain codebooks for near-field channel estimation and beam training: A comprehensive analysis, case studies, and implications for 6G,” *IEEE Signal Process. Mag.*, vol. 42, no. 1, pp. 45–59, 2025.
- [10] R.-C. Li, “Rayleigh quotient based optimization methods for eigenvalue problems,” *Matrix Functions and Matrix Equations*, vol. 19, pp. 76–108, 2015.

APPENDIX

Define $\Delta = m - n$, $\Sigma = m + n$, $\alpha = \frac{d^2}{2\lambda}$, $\beta = \frac{\lambda}{2}$. Then, we simplify (24) based on (21) and above definitions

$$A_{n,m} = \int_{\Omega_{\min}}^{\Omega_{\max}} e^{j2\pi\Delta\Omega} \int_{r_0^{\min}}^{r_0^{\max}} e^{j2\pi \frac{\Delta\Sigma}{r}(\beta\Omega^2 - \alpha)} dr d\Omega \\ \stackrel{(a)}{=} \int_{\Omega_{\min}}^{\Omega_{\max}} e^{j2\pi\Delta\Omega} \left[r e^{j\frac{C(\Omega)}{r}} - jC(\Omega) \text{Ei}\left(j\frac{C(\Omega)}{r}\right) \right]_{r_0^{\min}}^{r_0^{\max}} d\Omega,$$

where $C(\Omega) = 2\pi\Delta\Sigma(\beta\Omega^2 - \alpha)$, and $\text{Ei}(\cdot)$ denotes the exponential integral function. Step (a) follows by applying the identity $\int e^{j\frac{C}{r}} dr = r e^{j\frac{C}{r}} - C \text{Ei}\left(j\frac{C}{r}\right)$. The exponential integral term arises due to the nonlinear coupling between r and Ω , making a closed-form evaluation of the double integral intractable.

Instead we approximate $A_{n,m}$ numerically by computing Riemann sum over the angular parameter Ω and the range parameter r on the grid points (Ω_i, r_j) within the concentration region defined by $\Omega_i \in [\Omega_{\min}, \Omega_{\max}]$ and $r_j \in [r_0^{\min}, r_0^{\max}]$. The summation uses N_Ω samples along the angular (Ω) axis and N_r samples along the range (r) axis.

$$A_{n,m} \approx \sum_{i=1}^{N_\Omega} \sum_{j=1}^{N_r} b_n(\Omega_i, r_j) b_m^*(\Omega_i, r_j) \Delta\Omega \Delta r \quad (29)$$

where $\Delta\Omega$ and Δr denote the angular and range step sizes. Likewise, $B_{n,m}$ can be computed from (29), where the angle–range grid now spans the entire NF as defined in (25).